The Transiting Multi-planet System HD 3167: A 5.7 M _⊕ Super-Earth and an 8.3 M _⊕ Mini-Neptune

Gandolfi, D.; Barragán, O.; Hatzes, A.P.; Fridlund, M.; Fossati, L.; Donati, P.; ... ; Zakhozhay, O.V.

The Astronomical Journal, 154:123 (15pp), 2017 September https://doi.org/10.3847/1538-3881/aa832a

The Transiting Multi-planet System HD 3167: A 5.7 $M_\oplus$ Super-Earth and an 8.3 $M_\oplus$ Mini-Neptune

Davide Gandolfi[1], Oscar Barragán[1], Artie P. Hatzes[2], Malcolm Fridlund[3,4], Luca Fossati[5], Paolo Donati[6], Marshall C. Johnson[7], Grzegorz Nowak[8,9], Jorge Prieto-Arranz[8,9], Simon Albrecht[10], Fei Dai[11,12], Hans Deeg[8,9], Michael Endl[13], Sascha Grziwa[14], Maria Hjorth[10], Judith Korth[14], David Nespral[8,9], Joonas Saario[15], Alexis M. S. Smith[16], Giuliano Antoniciello[1], Javier Alarcon[17], Megan Bedell[18], Pere Blay[8,15], Stefan S. Brems[19], Juan Cabrera[16], Szilard Csizmadia[16], Felice Cusano[20], William D. Cochran[13], Philipp Eigmüller[16], Anders Erikson[16], Jonay I. González Hernández[8,9], Eike W. Guenther[2], Teruyuki Hirano[21], Alejandro Suárez Mascareño[8,22], Norio Narita[23,24,25], Enric Palle[8,9], Hannu Parviainen[8,9], Martin Pätzold[14], Carina M. Persson[4], Heike Rauer[16,26], Ivo Saviane[17], Linda Schmidtobreick[17], Vincent Van Eylen[3], Joshua N. Winn[11], and Olga V. Zakhozhay[27]

[1] Dipartimento di Fisica, Universitá di Torino, via P. Giuria 1, I-10125 Torino, Italy; davide.gandolfi@unito.it
[2] Thüringer Landessternwarte Tautenburg, Sternwarte 5, D-07778 Tautenberg, Germany
[3] Leiden Observatory, University of Leiden, PO Box 9513, 2300 RA, Leiden, The Netherlands
[4] Department of Earth and Space Sciences, Chalmers University of Technology, Onsala Space Observatory, SE-439 92 Onsala, Sweden
[5] Space Research Institute, Austrian Academy of Sciences, Schmiedlstrasse 6, A-8042, Graz, Austria
[6] INAF—Osservatorio Astrofisico di Arcetri, Largo E. Fermi 5, I-50125, Florence, Italy
[7] Department of Astronomy, The Ohio State University, 140 West 18th Avenue, Columbus, OH 43210, USA
[8] Instituto de Astrofísica de Canarias, C/ Vía Láctea s/n, E-38205 La Laguna, Spain
[9] Departamento de Astrofísica, Universidad de La Laguna, E-38206 La Laguna, Spain
[10] Stellar Astrophysics Centre, Department of Physics and Astronomy, Aarhus University, Ny Munkegade 120, DK-8000 Aarhus C, Denmark
[11] Department of Astrophysical Sciences, Princeton University, 4 Ivy Lane, Princeton, NJ 08544, USA
[12] Department of Physics and Kavli Institute for Astrophysics and Space Research, Massachusetts Institute of Technology, Cambridge, MA 02139, USA
[13] Department of Astronomy and McDonald Observatory, University of Texas at Austin, 2515 Speedway, Stop C1400, Austin, TX 78712, USA
[14] Rheinisches Institut für Umweltforschung an der Universität zu Köln, Aachener Strasse 209, D-50931 Köln, Germany
[15] Nordic Optical Telescope, Apartado 474, E-38700, Santa Cruz de La Palma, Spain
[16] Institute of Planetary Research, German Aerospace Center, Rutherfordstrasse 2, D-12489 Berlin, Germany
[17] European Southern Observatory, Alonso de Cordova 3107, Santiago, Chile
[18] Department of Astronomy and Astrophysics, University of Chicago, 5640 S. Ellis Avenue, Chicago, IL 60637, USA
[19] Landessternwarte Königstuhl, Zentrum für Astronomie der Universität Heidelberg, Königstuhl 12, D-69117, Heidelberg, Germany
[20] INAF—Osservatorio Astronomico di Bologna, Via Ranzani, 1, I-20127, Bologna, Italy
[21] Department of Earth and Planetary Sciences, Tokyo Institute of Technology, 2-12-1 Ookayama, Meguro-ku, Tokio 152-8551, Japan
[22] Observatoire Astronomique de l'Université de Genève, 1290 Versoix, Switzerland
[23] Department of Astronomy, The University of Tokyo, 7-3-1 Hongo, Bunkyo-ku, Tokyo 113–0033, Japan
[24] Astrobiology Center, NINS, 2-21-1 Osawa, Mitaka, Tokyo 181–8588, Japan
[25] National Astronomical Observatory of Japan, NINS, 2-21-1 Osawa, Mitaka, Tokyo 181–8588, Japan
[26] Center for Astronomy and Astrophysics, TU Berlin, Hardenbergstr. 36, D-10623 Berlin, Germany
[27] Main Astronomical Observatory, National Academy of Sciences of the Ukraine, 27 Akademika Zabolotnoho St. 03143, Kyiv, Ukraine
Received 2017 May 22; revised 2017 July 20; accepted 2017 July 25; published 2017 August 31

Abstract

HD 3167 is a bright ($V = 8.9$ mag) K0 V star observed by NASA's *K2* space mission during its Campaign 8. It has recently been found to host two small transiting planets, namely, HD 3167b, an ultra-short-period (0.96 days) super-Earth, and HD 3167c, a mini-Neptune on a relatively long-period orbit (29.85 days). Here we present an intensive radial velocity (RV) follow-up of HD 3167 performed with the FIES@NOT, HARPS@ESO-3.6 m, and HARPS-N@TNG spectrographs. We revise the system parameters and determine radii, masses, and densities of the two transiting planets by combining the *K2* photometry with our spectroscopic data. With a mass of $5.69 \pm 0.44\,M_\oplus$, a radius of $1.574 \pm 0.054\,R_\oplus$, and a mean density of $8.00^{+1.10}_{-0.98}$ g cm^{-3}, HD 3167b joins the small group of ultra-short-period planets known to have rocky terrestrial compositions. HD 3167c has a mass of $8.33^{+1.79}_{-1.85}\,M_\oplus$ and a radius of $2.740^{+0.106}_{-0.100}\,R_\oplus$, yielding a mean density of $2.21^{+0.56}_{-0.53}$ g cm^{-3}, indicative of a planet with a composition comprising a solid core surrounded by a thick atmospheric envelope. The rather large pressure scale height (~350 km) and the brightness of the host star make HD 3167c an ideal target for atmospheric characterization via transmission spectroscopy across a broad range of wavelengths. We found evidence of additional signals in the RV measurements but the currently available data set does not allow us to draw any firm conclusions on the origin of the observed variation.

Key words: planets and satellites: detection – planets and satellites: individual (HD 3167b, HD 3167c) – stars: fundamental parameters – stars: individual (HD 3167)

Supporting material: machine-readable table

1. Introduction

Back in 1995, the discovery of 51 Peg b demonstrated that gas-giant planets ($R_p \approx 1\,R_{Jup}$) could have orbital periods of a few days and thus exist quite close to their host star (Mayor & Queloz 1995). Space-based transit search missions such as *CoRoT* (Baglin & Fridlund 2006), *Kepler* (Borucki et al. 2010),

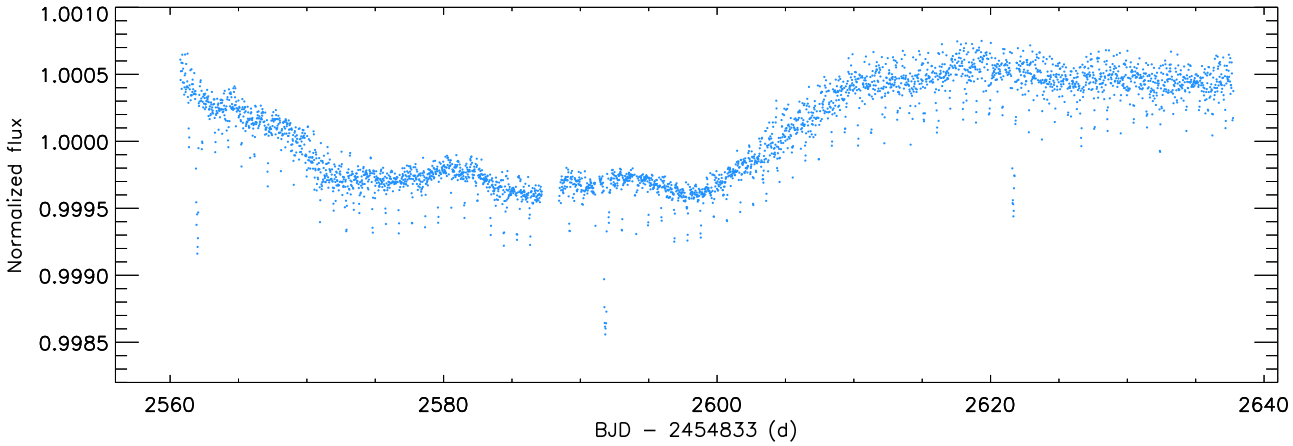

Figure 1. *K2* light curve of HD 3167 from Vanderburg et al. (2016).

and *K2* (Howell et al. 2014) have established that these close-in planets can have radii down to Neptune-like (Barragán et al. 2016; David et al. 2016) and even Earth-like values (Howard et al. 2009; Queloz et al. 2009; Pepe et al. 2013). Close-in exoplanets have challenged planet formation theories and play an important role in the architecture of exoplanetary systems (e.g., Winn & Fabrycky 2015; Hatzes 2016).

Based on the occurrence rate of planets and planet candidates discovered by *Kepler*, we know that short-period super-Earths ($R_p = 1$–$2\,R_\oplus$, $M_p = 1$–$10\,M_\oplus$) and sub-Neptunes ($R_p = 2$–$4\,R_\oplus$, $M_\oplus = 10$–$40\,M_\oplus$) are extremely common in our Galaxy. About 26% of solar-like stars in the Milky Way host small planets ($R_p < 4\,R_\oplus$) with orbital periods shorter than 100 days (see, e.g., Marcy et al. 2014; Burke et al. 2015). These planets are not represented in our solar system and were therefore completely unknown to us until a few years ago.

Although *Kepler* has provided us with a bonanza of such small planets, little is known about their masses, compositions, and internal structures. Mass determinations with a precision that allows us to distinguish between different internal compositions (better than 20%) have been possible only for a few dozen super-Earths and sub-Neptunes. The small radial velocity (RV) variation induced by such planets and the faintness of most *Kepler* host stars ($V > 13$ mag) make RV follow-up observations difficult. These observations either place too much demand on telescope time, or they are simply unfeasible with state-of-the-art facilities.

A special class of close-in objects is composed of exoplanets with ultra-short orbital periods ($P_{orb} < 1$ day; Sanchis-Ojeda et al. 2014). These planets are the most favorable cases for transit and RV search programs, as the transit probability is high ($\propto P_{orb}^{-2/3}$) and the induced RV variation is large ($\propto P_{orb}^{-1/3}$). Very short orbital periods are also advantageous because they are (often) much shorter than the rotation period of the star, allowing the correlated noise due to stellar rotation to be more easily distinguished from the planet-induced RV signal (Hatzes et al. 2011). To date, about 80 ultra-short-period exoplanets have been discovered,[28] mainly from transit surveys starting with CoRoT-7b (Léger et al. 2009). Masses, however, have only been determined for two dozen of these objects. About half of these are gas-giant planets with masses between 1 and 10 M_{Jup}. The rest are small planets in the super-earth regime with masses between about 5 and 10 $M_\oplus$.

Using time-series photometric data from the *K2* space mission, Vanderburg et al. (2016) recently announced the discovery of two small transiting planets around the bright ($V = 8.9$ mag) K0 dwarf star HD 3167. The inner planet, HD 3167b, has a radius of $R_p = 1.6\,R_\oplus$ and transits the host star every 0.96 days. By our definition, HD 3167b qualifies as an ultra-short-period planet. The outer planet, HD 3167c, has a radius of $2.9\,R_\oplus$ and an orbital period of 29.85 days. The brightness of the host star makes the system amenable to follow-up observations such as high-precision RV measurements for planetary mass determination.

As part of the ongoing RV follow-up program of *K2* transiting planets successfully carried out by our consortium KESPRINT (e.g., Sanchis-Ojeda et al. 2015; Grziwa et al. 2016; Van Eylen et al. 2016; Barragán et al. 2017; Fridlund et al. 2017; Guenther et al. 2017; Nowak et al. 2017), we herein present the results of an intensive RV campaign we conducted with the FIES, HARPS, and HARPS-N spectrographs to accurately measure the masses of the two small planets transiting HD 3167. The paper is organized as follows. In Sections 2 and 3, we provide a short recap of the *K2* data and describe our high-resolution spectroscopic observations. The properties of the host star are reported in Section 4. We present the data modeling in Section 5 along with the frequency analysis of our RV time-series. Results, discussions, and summary are given in Sections 6 and 7.

2. *K2* Photometry

K2 observed HD 3167 during its Campaign 8 for about 80 days—between 2016 January and March—with an integration time of about 29.4 minutes (long cadence mode). For our analysis presented in Sections 4.3 and 5.3, we used the light curve extracted following the technique described in Vanderburg & Johnson (2014).[29] We refer the reader to Vanderburg et al. (2016) for a detailed description of both the *K2* data of HD 3167 and the detection of the two transiting planets. For the sake of clarity, we reproduce in Figure 1 the full light curve of HD 3167 presented in Vanderburg et al. (2016).

3. Spectroscopic Follow-up

We used the FIbre-fed Échelle Spectrograph (FIES; Frandsen & Lindberg 1999; Telting et al. 2014) mounted at the 2.56 m Nordic Optical Telescope (NOT) of Roque de los Muchachos Observatory (La Palma, Spain) to acquire 37 high-resolution

[28] See exoplanets.org and exoplanet.eu; as of 2017 May.

[29] Publicly available at https://www.cfa.harvard.edu/~avanderb/k2.html.

Table 1
Spectroscopic Parameters of HD 3167 as Derived from the FIES (Top), HARPS (Middle), and HARPS-N (Bottom) Data Using the Three Methods Described in Section 4.1

Method	$T_{\rm eff}$ (K)	$\log g_\star$ (cgs)	[Fe/H] (dex)	$v_{\rm mic}$ (km s^{-1})	$v_{\rm mac}$ (km s^{-1})	$v \sin i_\star$ (km s^{-1})
FIES						
Method 1	5288 ± 75	4.53 ± 0.07	0.02 ± 0.06	0.9 ± 0.1	2.3 ± 0.5	1.9 ± 0.8
Method 2	5270 ± 95	4.56 ± 0.10	0.05 ± 0.05	0.9 ± 0.1	2.3 ± 0.6	1.7 ± 0.6
Method 3	5247 ± 76	4.44 ± 0.19	0.01 ± 0.10	0.7 ± 0.2	...	...
HARPS						
Method 1	5295 ± 70	4.54 ± 0.05	0.03 ± 0.05	0.9 ± 0.1	2.4 ± 0.5	1.8 ± 0.6
Method 2	5230 ± 80	4.54 ± 0.07	0.05 ± 0.06	0.9 ± 0.1	2.3 ± 0.5	1.7 ± 0.6
Method 3	5257 ± 112	4.41 ± 0.20	0.04 ± 0.08	0.8 ± 0.1	...	...
HARPS-N						
Method 1	5275 ± 62	4.51 ± 0.05	0.03 ± 0.05	0.9 ± 0.1	2.4 ± 0.5	1.7 ± 0.6
Method 2	5260 ± 70	4.52 ± 0.06	0.04 ± 0.05	0.9 ± 0.1	2.3 ± 0.5	1.8 ± 0.6
Method 3	5247 ± 121	4.40 ± 0.20	0.06 ± 0.09	0.7 ± 0.1	...	...

spectra ($R \approx 67{,}000$) in 12 different nights between July and September 2016. FIES is mounted inside a heavily insulated building separate from the dome to isolate the spectrograph from sources of thermal and mechanical instability. The temperature inside the building is kept constant within 0.02°C. Observations of RV standard stars performed by our team since 2011, have shown that long-exposed ThAr spectra taken immediately before and after short-exposed targets' observations ($T_{\rm exp} \leqslant 20$ minutes) allow us to trace the intra-night RV drift of the instrument to within $\sim$2–3 m s^{-1} (Gandolfi et al. 2013, 2015), which is comparable to the internal precision of our FIES RV measurements (Table 5). On the other hand, observations of standard stars performed in different nights have shown that the inter-night stability of the instrument is two to four times worse.

The FIES observations were carried out as part of the OPTICON and NOT observing programs 16A/055, P53-016, and P53–203. We set the exposure time to 15–20 minutes and acquired long-exposed ($T_{\rm exp} \approx 35$ seconds) ThAr spectra immediately before and after the target observations. We took at least two spectra separated by 1–2 hr per night except on one night. The data were reduced using standard routines, which include bias subtraction, flat fielding, order tracing and extraction, and wavelength calibration. Radial velocities were derived via multi-order cross-correlations, using the stellar spectrum with the highest signal-to-noise ratio (S/N) as a template.[30] The measured RVs are listed in Table 5 along with their 1σ internal uncertainties and the S/N per pixel at 5500 Å.

We also acquired 50 spectra with the HARPS spectrograph ($R \approx 115{,}000$; Mayor et al. 2003) and 32 spectra with the HARPS-N spectrograph ($R \approx 115{,}000$; Cosentino et al. 2012). HARPS and HARPS-N are fiber-fed cross-dispersed echelle spectrographs specifically designed to achieve very high-precision long-term RV stabilities (<1 m s^{-1}). They are mounted at the ESO-3.6 m telescope of La Silla observatory (Chile) and at the 3.58 m Telescopio Nazionale Galileo (TNG) of Roque de los Muchachos Observatory (La Palma, Spain).

The HARPS and HARPS-N observations were performed as part of the ESO observing programs 097.C-0948 and 098.C-0860, and of the TNG/CAT programs A33TAC_15 and CAT16B_61. We used the simultaneous Fabry–Perot calibrator and set the exposure times to 15–40 minutes depending on sky conditions and scheduling constraints. We followed the same multi-visit strategy adopted for the FIES observations, i.e., we acquired at least two spectra per night in most of the observing nights. The data were reduced using the dedicated HARPS and HARPS-N off-line pipelines and radial velocities were extracted by cross-correlating the extracted echelle spectra with a G2 numerical mask. We also tested the K0 and the K5 mask but found neither a significant improvement of the error bars, nor a significant variation of the relative amplitude of the detected RV variation.

The HARPS and HARPS-N RV measurements and their uncertainties are also listed in Table 5, along with the S/N per pixel at 5500 Å, the full-width half maximum (FWHM) and bisector span (BIS) of the cross-correlation function (CCF), and the Ca II H & K chromospheric activity index $\log R'_{\rm HK}$. Five out of the 50 HARPS spectra are affected by poor sky and seeing conditions. They are not listed in Table 5 and were not used in our analysis.

4. Stellar Properties

4.1. Spectroscopic Parameters

We combined separately the FIES, HARPS, and HARPS-N data to produce three co-added spectra of higher S/N and determine the spectroscopic parameters of the host star. The stacked FIES, HARPS, and HARPS-N spectra have S/N of 500, 560, and 480 per pixel at 5500 Å, respectively. We derived the spectroscopic parameters using three independent methods as described in the next three paragraphs. Results for each method and spectrum are listed in Table 1.

Method 1. This uses a customized `IDL` software suite that implements the spectral synthesis program `SPECTRUM`[31] (V2.76; Gray & Corbally 1994) to compute synthetic spectra using `ATLAS 9` model atmospheres (Castelli & Kurucz 2004). The code fits spectral features that are sensitive to different photospheric parameters, adopting the calibration equations of Bruntt et al. (2010) and Doyle et al. (2014) to determine the microturbulent ($v_{\rm mic}$) and macroturbulent ($v_{\rm mac}$) velocities. It uses the wings of the Balmer lines to obtain a first guess of the effective temperature ($T_{\rm eff}$), and the Mg I 5167, 5173, 5184 Å, the Ca I 6162, 6439 Å, and the Na I D lines to refine the

[30] Epoch 2457605.

[31] Publicly available at http://www.appstate.edu/~grayro/spectrum/spectrum.html.

Table 2
Stellar Parameters

Parameter	Value
Effective temperature $T_{\rm eff}$ (K)	5286 ± 40
Surface gravity[a] $\log g_\star$(cgs)	4.53 ± 0.03
Surface gravity[b] $\log g_\star$(cgs)	4.51 ± 0.03
Iron abundance [Fe/H] (dex)	0.03 ± 0.03
Projected rot. velocity $v \sin i_\star$(km s^{-1})	1.8 ± 0.4
Interstellar extinction $A_{\rm v}$ (mag)	0.02 ± 0.03
Stellar mass $M_\star$ ($M_\odot$)	0.877 ± 0.024
Stellar radius $R_\star$ ($R_\odot$)	0.835 ± 0.026
Age (Gyr)	5 ± 4
Rotation period $P_{\rm rot}$ (day)	23.52 ± 2.87
Distance[c] (pc)	45.8 ± 2.2

Notes.
[a] From spectroscopy.
[b] From spectroscopy and isochrones.
[c] Hipparcos' distance from van Leeuwen (2007).

effective temperature estimate and derive the surface gravity ($\log g_\star$). The iron abundance [Fe/H] and projected rotational velocity $v \sin i_\star$ are measured by fitting many isolated and unblended iron lines.

Method 2. This uses the spectral analysis package SME (V4.43; Valenti & Piskunov 1996; Valenti & Fischer 2005) along with both ATLAS 12 and MARCS model atmospheres (Gustafsson et al. 2008; Kurucz 2013). SME calculates synthetic spectra and fits them iteratively to the observed high-resolution echelle spectra using a chi-squared minimization procedure. Micro and macroturbulent velocities are estimated using the same calibration equations adopted by the first method. $T_{\rm eff}$, $\log g_\star$, [Fe/H], and $v \sin i_\star$ are derived by fitting the same spectral features as in the previous paragraph.

Method 3. This is based on the classical equivalent width (EW) technique applied to about 100 Fe I and 10 Fe II lines. It uses the public version of the line list prepared for the *Gaia*-ESO Survey (Heiter et al. 2015), which is based on the VALD3 atomic database (Ryabchikova et al. 2011). $T_{\rm eff}$ is obtained by removing trends between the abundance of a given element and the respective excitation potential; $\log g_\star$ is derived by assuming the ionization equilibrium condition, i.e., by requiring that for a given species the same abundance (within the uncertainties) is obtained from lines of two ionization states (typically neutral and singly ionized species); $v_{\rm mic}$ and [Fe/H] are estimated by minimizing the slope of the relationship between abundance and the logarithm of the reduced EWs. Equivalent widths are measured using the code DOOp (Cantat-Gaudin et al. 2014), a wrapper of DAOSPEC (Stetson & Pancino 2008). The photospheric parameters are derived with the code FAMA (Magrini et al. 2013), a wrapper of MOOG (Sneden et al. 2012).

The three techniques provide consistent results, regardless of the used spectrum and/or method. While we have no reason to prefer one method over the other, we adopted the results of *Method 1* applied on the FIES, HARPS, and HARPS-N spectra. The final adopted values for $T_{\rm eff}$, $\log g_\star$, [Fe/H], and $v \sin i_\star$ are the averaged estimates we obtained using the first method; the corresponding uncertainties are defined as the square root of the individual errors added in quadrature, divided by three. We obtained $T_{\rm eff} = 5286 \pm 40$ K, $\log g_\star = 4.53 \pm 0.03$ (cgs), [Fe/H] $= 0.03 \pm 0.03$ dex, and $v \sin i_\star = 1.8 \pm 0.4$ km s^{-1}(Table 2). Our results are in fairly good agreement with the spectroscopic parameters derived by Vanderburg et al. (2016).

4.2. Stellar Mass, Radius, and Age

We followed the same method adopted by Vanderburg et al. (2016) and derived the mass, radius, and age of HD 3167 using PARAM, an online interface for Bayesian estimation of stellar parameters.[32] Briefly, PARAM interpolates the apparent visual magnitude, parallax, effective temperature and iron abundance onto PARSEC model isochrones (Bressan et al. 2012), adopting the initial mass function from Chabrier (2001). We used our spectroscopic parameters (Section 4.1) along with the *V*-band magnitude listed in the EPIC input catalog ($V = 8.941 \pm 0.015$ mag) and the *Hipparcos*' parallax (21.82 ± 1.05 mas, van Leeuwen 2007).[33] Following the method outlined in Gandolfi et al. (2008) and using the broadband photometry available in the EPIC input catalog, we found that the reddening is consistent with zero ($A_{\rm v} = 0.02 \pm 0.03$ mag), as expected given the short distance to the star (45.8 ± 2.2 pc). We thus set the interstellar absorption to zero and did not correct the apparent visual magnitude.

HD 3167 has a mass of $M_\star = 0.877 \pm 0.024\ M_\odot$ and a radius of $R_\star = 0.835 \pm 0.026\ R_\odot$, implying a surface gravity of $\log g_\star = 4.51 \pm 0.03$ (cgs), in agreement with the spectroscopically derived value (Section 4.1). The isochrones constrain the age of the star to be 5 ± 4 Gyr.

4.3. Stellar Activity and Rotation Period

The average Ca II H & K activity index $\log R'_{\rm HK}$, as measured from the HARPS and HARPS-N spectra, is -5.03 ± 0.01 and -5.06 ± 0.02 dex, respectively, indicative of a low chromospheric activity level.[34] We checked if the extrinsic absorption, either from the interstellar medium (ISM) or from material local to the system, biases the measured values of $\log R'_{\rm HK}$ (Fossati et al. 2013, 2015). The far-ultraviolet (FUV) stellar emission, which originates in the chromosphere and transition region, provides instead an unbiased measure of the stellar activity (Fossati et al. 2015). We measured the excess of the chromospheric FUV emission—directly proportional to stellar activity—by estimating the difference between the measured *GALEX* FUV flux and the photospheric flux derived from a MARCS model with the same photospheric parameters as the star (Gustafsson et al. 2008) rescaled to fit the observed optical (Johnson and Tycho) and infrared (2MASS and *WISE*) photometry of HD 3167. The fit accounts for the interstellar extinction reported in Section 4.2. We obtained an excess emission in the *GALEX* FUV band of about 260 erg cm^{-2} s^{-1}, indicative of a low level of stellar activity (Shkolnik et al. 2014), in agreement with the $\log R'_{\rm HK}$ value. This provides evidence that the Ca II activity index $\log R'_{\rm HK}$ is very likely not biased by extrinsic absorption.

The light curve of HD 3167 displays a 0.08% flux drop occurring during the first half of the *K2* observations and lasting for about 35–40 days (Figure 1). If the variation were due to an active region moving in and out of sight as the star

[32] Available at http://stev.oapd.inaf.it/cgi-bin/param.
[33] *Gaia*'s first data release does not report the parallax of HD 3167.
[34] As a comparison, the activity index of the Sun varies between −5.0 and −4.8 dex.

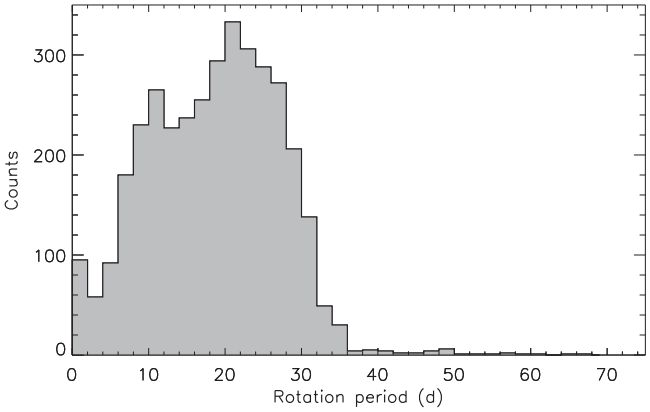

Figure 2. Rotation period distribution of *Kepler* field stars with $5170 \leqslant T_{\rm eff} \leqslant 5370$ K and $\log g_\star \geqslant 4.3$ (cgs), as extracted from the work of McQuillan et al. (2014).

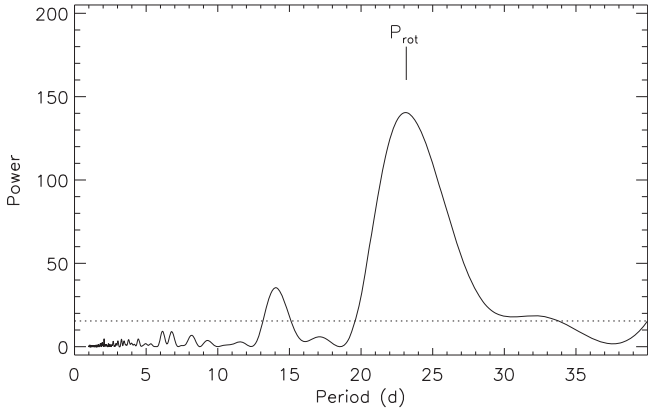

Figure 3. Lomb–Scargle periodogram of the *K2* light curve of HD 3167. The horizontal dashed line marks the 0.1% FAP as defined in Scargle (1982).

rotates around its axis, then the rotation period of the star should be at least twice as long, i.e., 70–80 days. Such a long rotation period seems to be unlikely for a K-type dwarf and is inconsistent with our $v \sin i_\star$ measurement and stellar radius determination (see below). Figure 2 shows the distribution of the rotation period of 3591 late G-and early K-type dwarfs as measured by McQuillan et al. (2014) using *Kepler* light curves. We selected only *Kepler* stars with photospheric parameters similar to those of HD 3167, i.e., objects with $5170 \leqslant T_{\rm eff} \leqslant 5370$ K and $\log g_\star \geqslant 4.40$ (cgs). None of the "HD 3167's *Kepler* twins" has a rotation period longer than 70 days. Moreover, only nine objects have a rotational period exceeding 50 days. As the K2 light curves of HD 3167 from Luger et al. (2016) and Aigrain et al. (2016) display the same feature, we conclude that the observed 0.08% flux drop is very likely an instrumental artifact caused by the spacecraft pointing jitter, rather than the way the time-series data have been extracted.

Figure 3 shows the Lomb–Scargle (LS) periodogram (Lomb 1976; Scargle 1982) of the *K2* light curve of HD 3167 following the subtraction of the best-fitting transit models of planets b and c (Section 5). Besides a very strong peak at ∼75 days due to the flux drop described in the previous paragraph, there are two additional significant peaks at 14 and 23.5 days with a Scargle's false alarm probability (FAP) lower than 0.1%. Since the period ratio is close to 0.5, we interpreted the former as the first harmonic of the latter. With an amplitude of about 0.04%, the 23.5 day signal is clearly visible in the first half of the *K2* time-series data, whereas it is barely visible in the second half of the photometric data (Figure 1). As a sanity check, we split the light curve into two chunks of ∼40 days and calculated the LS periodogram of each chunk. The 23.5 day signal is detected also in the second half of the light curve but with a lower significance. This is likely due to the 80% higher noise level of the second half of the *K2* data with respect to the first half, as pointed out by Vanderburg et al. (2016).

We interpreted the 23.5 day signal as the rotation period of the star and attributed the peak at 14 days to the presence of active regions located at opposite stellar longitudes. We measured a rotation period and uncertainty of $P_{\rm rot} = 23.52 \pm 2.87$ days defined as the position and full width at half maximum of the corresponding peak in the LS periodogram. If the rotation period of the star were instead 14 days, the magnetic activity of the star would very likely be stronger than what has been measured from the $\log R'_{\rm HK}$ activity index (Suárez Mascareño et al. 2015). It is also worth noting that the distribution of the rotational periods of HD 3167's *Kepler* twins is peaked between 20 and 25 days (Figure 2).

The spectroscopically derived projected rotational velocity of the star $v \sin i_\star = 1.8 \pm 0.4$ km s^{-1}, combined with the stellar radius $R_\star = 0.835 \pm 0.026\ R_\odot$, implies an upper limit on the rotation period of 23.5 ± 5.3 days, in agreement with the period derived from the K2 light curve, further corroborating our results. This also suggests that the star is seen nearly equator-on and that the transiting multi-planet system around HD 3167 might be aligned along the line of sight.

5. Data Analysis

5.1. Periodogram Analysis of the Radial Velocities

We first performed a frequency analysis of the RV measurements in order to look for possible periodic signals in the data and assess if, in the absence of the K2 transit photometry, we would have been able to detect the presence of HD 3167b and c. For this purpose, we used only the HARPS and HARPS-N measurements because of the higher quality and superb long-term stability of the two instruments.

We first analyzed the two data sets separately to account for the velocity offset between the two spectrographs. Although HARPS and HARPS-N are very similar, a small offset (<10 m s^{-1}) is expected given, e.g., the different detector, optics, wavelength coverage of the two instruments. The generalized Lomb–Scargle (GLS; Zechmeister & Kürster 2009) periodograms of the HARPS and HARPS-N RVs show a significant peak at the orbital period of HD 3167b, with an FAP[35] of about 10^{-5} and 10^{-7}, respectively (top and middle panels of Figure 4). We conclude that the signal of the inner planet HD 3167b is clearly present in both data sets. The GLS periodogram of the HARPS data displays a significant peak at ∼32 days (FAP $= 10^{-4}$), which is close to the orbital period of HD 3167c (29.85 days). However, the outer transiting planet remains undetected in the HARPS-N data, owing to the uneven sampling of the orbital phase of the outer transiting planet with this instrument (Figure 9).

[35] The FAPs reported in this subsection have been calculated using Equation (24) of Zechmeister & Kürster (2009) and should be regarded as preliminary estimates. Deriving reliable FAPs through a bootstrap analysis—as presented in Section 5.4—goes beyond the scope of this subsection.

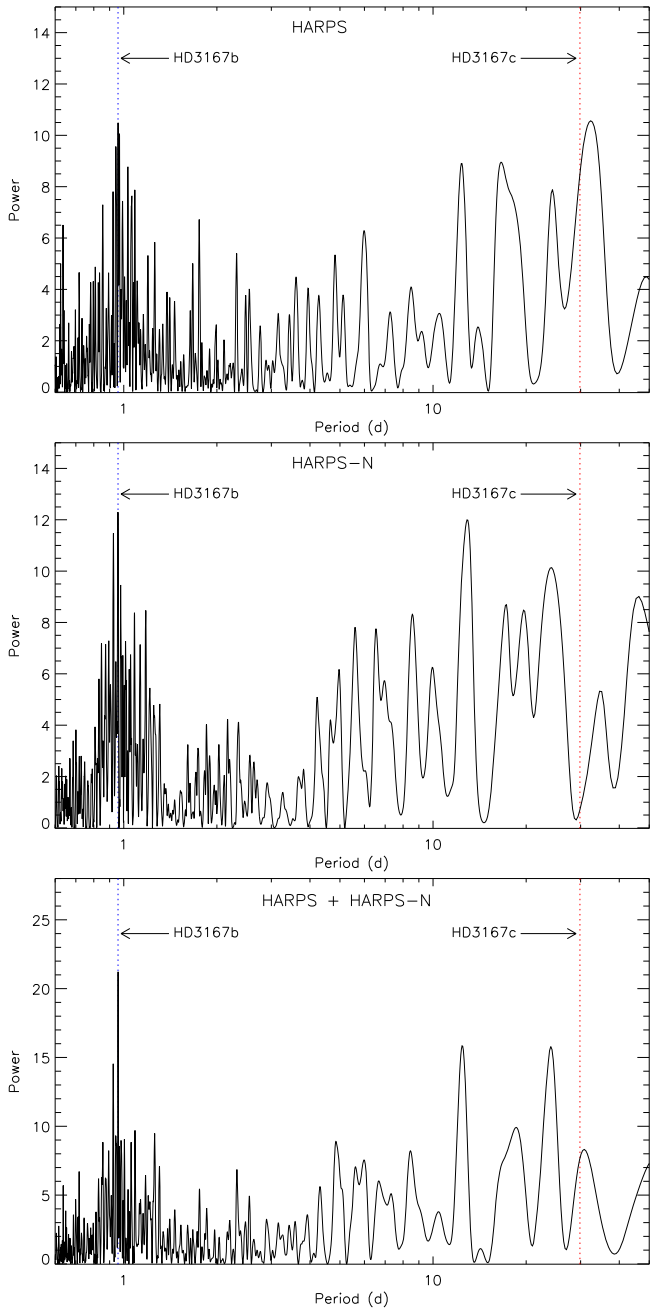

Figure 4. GLS periodograms of the HARPS (top panel), HARPS-N (middle panel), and HARPS+HARPS-N (bottom panel) RV measurements. The vertical dashed lines mark the orbital periods of HD 3167b (0.96 days) and HD 3167c (29.85 days).

On three occasions,[36] we observed HD 3167 nearly simultaneously (within 10 minutes) with HARPS and HARPS-N. We used these measurements to measure the offsets of the RV, FWHM, BIS, and $\log R'_{\rm HK}$ between the two data sets and calculate the periodograms of the combined data. We found $\Delta\,{\rm RV}_{\rm (HS\text{-}HN)} = 8.0 \pm 0.5\,{\rm m\,s^{-1}}$, $\Delta\,{\rm FWHM}_{\rm (HS\text{-}HN)} = 0.068 \pm 0.006\,{\rm km\,s^{-1}}$, $\Delta\,{\rm BIS}_{\rm (HS\text{-}HN)} = 0.009 \pm 0.003\,{\rm km\,s^{-1}}$, and $\Delta \log R'_{\rm HK(HS-HN)} = -0.030 \pm 0.005$. We stress that these offsets have only been used to perform the periodogram analysis of the joint data.

[36] Epochs 2457611, 2457646, and 2457692.

As expected, the GLS periodogram of the joint data set (bottom panel of Figure 4) shows a very significant peak at the orbital period of the inner planet HD 3167b (FAP $= 10^{-10}$) and a moderately significant peak at the orbital period of HD 3167c.

It is worth noting that the three periodograms also show the presence of a significant peak at 23.8 days (0.042 c/d), which is close to the rotation period of the star. We stress, however, that this peak corresponds to the 1 day alias of the orbital period of HD 3167b. The periodogram of the RV residuals—as obtained following the subtraction of the signals of the two planets—show no peaks at 0.042 c/d (Figure 6), as expected for alias frequencies (see, e.g., Section 5.4).

5.2. Orbital Solution of HD 3167b

We performed a Keplerian fit of the FIES, HARPS, and HARPS-N RV data following the floating chunk offset (FCO) method described in Hatzes et al. (2011). The FCO method exploits the reasonable assumption that, for ultra-short-period planets, RV measurements taken on a single night mainly reflect the orbital motion of the planet rather than other, longer period phenomena such as stellar rotation, magnetic activity, and additional planets. If we can sample a sufficient time segment of the Keplerian curve, then these nightly "chunks" can be shifted until the best fit to the orbital motion is found. This method was successfully used to determine the mass of the ultra-short-period planets CoRoT-7b (Hatzes et al. 2011) and Kepler-78b (Hatzes 2014).

The ultra-short-period planet HD 3167b is well suited for application of the FCO method. This technique is particularly effective at filtering out the long-term RV variation due to magnetic activity coupled with stellar rotation. The star has an estimated rotation period of about 23.5 days (Section 4.3), which is longer than the orbital period of HD 3167b. Although HD 3167 is a relatively inactive star (Section 4.3), the FCO method helps in filtering out even a small amount of spot-induced RV variability. HD 3167c has an orbital period of about 29.95 days, which results in a change of less than 0.01 in phase within the nightly visibility window of the target (∼5–6 hr). The RV of the star due to the outer transiting planet does not change significantly during an observing night. Moreover, each of the three data sets has its own zero-point offset, which is naturally taken into account by the method. Finally, the FCO technique also removes—or at least greatly minimizes—any long-term systematic errors, such as the night-to-night RV drifts of FIES (Section 3).

We modeled the FIES, HARPS, and HARPS-N RV measurements with our code `pyaneti`[37] (Barragán et al. 2016, 2017), an MCMC-based software suite that explores the parameter space using the ensemble sampler with the affine invariance algorithm (Goodman & Weare 2010). Following Hatzes et al. (2011), we divided the RVs into three subsets of nightly measurements—one per instrument—and analyzed only those radial velocities for which multiple measurements were acquired on the same night, leading to a total of 12, 15, and 11 chunks of nightly FIES, HARPS, and HARPS-N RVs, respectively. The best-fitting orbital solution of HD 3167b was found keeping period and transit ephemeris fixed to the values derived by our joint analysis described in Section 5.3, but allowing the RV semi-amplitude variation $K_{\rm b}$ and the 38 nightly offsets to vary. We also fitted for $\sqrt{e_{\rm b}}\sin\omega_{\star,{\rm b}}$ and

[37] Available at https://github.com/oscaribv/pyaneti.

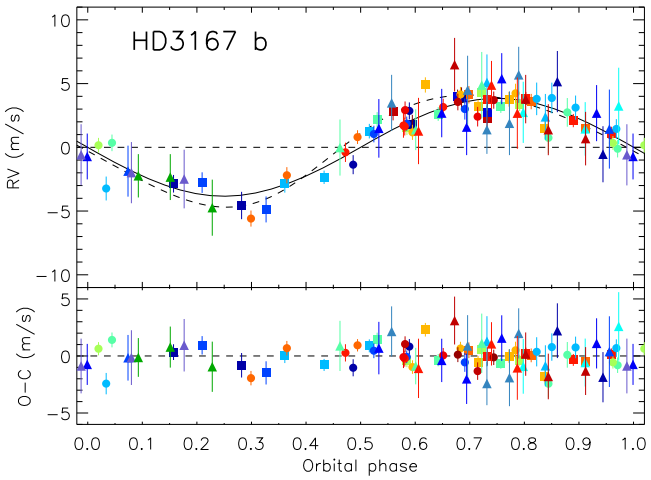

Figure 5. Upper panel: the RV curve of HD 3167 phase-folded to the orbital period of planet b, as derived using the FCO method. The best-fitting circular (adopted) and eccentric solutions are marked with a thick and dashed line, respectively. The FIES, HARPS, and HARPS-N RV measurements are plotted with triangles, circles, and squares, respectively, along with their formal error bars. Different colors represent measurements from different observing nights. Lower panel: residuals to the circular model.

$\sqrt{e_{\rm b}}\cos\omega_{\star,{\rm b}}$, where $e_{\rm b}$ is the eccentricity and $\omega_{\star,{\rm b}}$ is the argument of periastron of the star (Ford 2006). We also fitted for a constant white-noise term (commonly referred to as the RV "jitter" term) to account for instrumental velocity noise not included in the nominal uncertainties and/or possible sources of short-term stellar variability (such as granulation) not removed by the FCO method. Three independent jitters were added in quadrature to the formal error bars of each instrument (because it is not clear whether the jitter is astrophysical or instrumental in origin) and were allowed to vary in the fit so to yield $\chi^2/{\rm dof}=1$. We adopted uniform uninformative priors within a wide range for each parameter and ran 500 independent Markov chains. The burn-in phase was performed with 25,000 iterations using a thin factor of 50, leading to a posterior distribution of 250,000 independent data points for each fitted parameter. The final estimates and their 1σ uncertainties were taken as the median and 68% of the credible interval of the posterior distributions.

We obtained a best-fitting non-zero eccentricity of $e_{\rm b}=0.12\pm0.05$. We also fitted the RV data assuming a circular orbit ($\sqrt{e_{\rm b}}\sin\omega_{\star,{\rm b}}=\sqrt{e_{\rm b}}\cos\omega_{\star,{\rm b}}=0$). Figure 5 displays our FIES, HARPS, and HARPS-N measurements along with the best-fitting circular (thick line) and eccentric model (dashed line). Different symbols refer to different instruments, whereas different colors represent different nights. We note that the best-fitting eccentric solution might be driven by the uneven distribution of data points along the RV curve (Figure 5). In order to assess the significance of our result, we created 10^5 sets of synthetic RVs that sample the best-fitting circular solution at the epochs of our real observations. We added Gaussian noise at the same level of our measurements and fitted the simulated data allowing for an eccentric solution. We found that there is an $\sim$18% probability that a best-fitting eccentric solution with $e\geqslant0.12$ could have arisen by chance if the orbit were actually circular. Because this is above the 5% significance level suggested by Lucy & Sweeney (1971), we decided to conservatively assume a circular model. We found an RV semi-amplitude variation of $K_{\rm b}=3.81\pm0.50$ m s^{-1}, which translates into a mass of $M_{\rm b}=5.39\pm0.72\,M_\oplus$ for HD 3167b. We note that the eccentric solution provides a planetary mass that is consistent within 1σ with the result from the circular model.

Table 3
Low-mass ($M\lesssim8.4\,M_\oplus$) Planets with RV-determined Masses, $\Lambda\lesssim20$, and Bulk Densities Suggestive of a Mostly Rocky Composition (Mean Density $\rho_p>4$ g cm^{-3})

Planet	Λ	ρ_p g cm^{-3}
55 Cnc e	15.6	5.14
CoRoT-7 b	15.6	7.97
GJ 1132b	18.4	5.79
HD 219134b	20.6	5.94
Kepler-10 b	8.9	6.31
Kepler-78 b	5.5	6.43
Kepler-93 b	18.1	6.82
Kepler-97 b	12.3	5.93
HD 3167b	15.6	8.00

Note.
Except for HD 3167b, all values are taken from Cubillos et al. (2017).

5.3. Transit and RV Joint Analysis

We performed a joint modeling of the *K2* and RV measurements with `pyaneti`. The photometric data includes 6 and 15 hr of *K2* data points centered around each transit of HD 3167b and c. We detrended the segments using the program `exotrending`[38] (Barragán & Gandolfi 2017). Briefly, we fitted a second order polynomial to the out-of-transit data and removed outliers using a 3σ-clipping algorithm applied to the residuals of the preliminary best-fitting transit models derived using the formalism of Mandel & Agol (2002) coupled to a non-linear least square fitting procedure. As for the RV data sets, we used only the HARPS and HARPS-N measurements because of the long-term instability of the FIES spectrograph (Section 3).

We modeled the RV data with two Keplerian signals and fitted the transit light curves using the Mandel & Agol (2002)'s model with a quadratic limb-darkening law. We parametrized the limb-darkening coefficients following (Kipping 2013). To account for the *K2* long cadence data, we integrated the transit models over 10 steps. We adopted the same Gaussian likelihood as defined in Barragán et al. (2016). For each planet i we fitted for the orbital period $P_{{\rm orb},i}$, time of first transit $T_{0,i}$, scaled semimajor axis $a_i/R_\star$, impact parameter b_i, planet-to-star radius ratio $R_{\rm i}/R_\star$, and RV semi-amplitude variation K_i. To account for the RV offset between HARPS and HARPS-N, we fitted also for a systemic velocity for each instrument. We assumed a circular orbit for the inner planet and fitted for $\sqrt{e_c}\sin\omega_{\star,c}$ and $\sqrt{e_c}\cos\omega_{\star,c}$ for the outer planet.

The 30-minute integration time of *K2* smears out the shape of planetary transits increasing the degeneracy between the scaled semimajor axis $a/R_\star$ and the impact parameter b (Csizmadia et al. 2011). We therefore set Gaussian priors for the stellar mass and radius using the values derived in Section 4.2 and constrained $a_{\rm i}/R_\star$ of both planets from their

[38] Available at https://github.com/oscaribv/exotrending.

Table 4
System Parameters

Parameter	Prior[a]	Value
Model parameters for HD 3167b		
Orbital period $P_{\rm orb}$ (day)	$\mathcal{U}$[0.9596, 0.9598]	0.959632 ± 0.000015
Transit epoch T_0 ($BJD_{TDB}-2{,}450{,}000$)	$\mathcal{U}$[7394.3675, 7394.3763]	$7394.37442^{+0.00060}_{-0.00055}$
Scaled semimajor axis $a/R_\star$	$\mathcal{N}$[4.74, 0.18]	$4.516^{+0.076}_{-0.085}$
Scaled planet radius $R_{\rm p}/R_\star$	$\mathcal{U}$[0, 0.5]	0.01728 ± 0.00025
Impact parameter, b	$\mathcal{U}$[0, 1]	$0.11^{+0.11}_{-0.08}$
Radial velocity semi-amplitude variation K (m s^{-1})	$\mathcal{U}$[0, 100]	4.02 ± 0.31
$\sqrt{e}\sin\omega$	$\mathcal{F}$[0]	0
$\sqrt{e}\cos\omega$	$\mathcal{F}$[0]	0
Derived parameters for HD 3167b		
Planet mass $M_{\rm p}$ ($M_\oplus$)	...	5.69 ± 0.44
Planet radius $R_{\rm p}$ ($R_\oplus$)	...	1.574 ± 0.054
Mean density $\rho_{\rm b}$ (g cm^{-3})	...	$8.00^{+1.10}_{-0.98}$
Eccentricity e	...	0 (fixed)
Semimajor axis of the planetary orbit a (au)	...	0.01752 ± 0.00063
Orbit inclination $i_{\rm p}$ (°)	...	$88.6^{+1.0}_{-1.4}$
Transit duration τ_{14} (hr)	...	1.65 ± 0.03
Equilibrium temperature[b] $T_{\rm eq}$ (K)	...	1759 ± 20
Model parameters for HD 3167c		
Orbital period $P_{\rm orb}$ (day)	$\mathcal{U}$[29.8508, 29.8532]	$29.84622^{+0.00098}_{-0.00091}$
Transit epoch T_0 ($BJD_{TDB}-2{,}450{,}000$)	$\mathcal{U}$[7394.9763, 7394.9787]	7394.97831 ± 0.00085
Scaled semimajor axis $a/R_\star$	$\mathcal{N}$[46.3, 1.4]	46.5 ± 1.5
Scaled planet radius $R_{\rm p}/R_\star$	$\mathcal{U}$[0, 0.5]	$0.03006^{+0.00065}_{-0.00055}$
Impact parameter, b	$\mathcal{U}$[0, 1]	$0.30^{+0.11}_{-0.18}$
Radial velocity semi-amplitude variation K (m s^{-1})	$\mathcal{U}$[0, 100]	$1.88^{+0.40}_{-0.42}$
$\sqrt{e}\sin\omega$	$\mathcal{U}$[−1, 1]	$0.00^{+0.17}_{-0.24}$
$\sqrt{e}\cos\omega$	$\mathcal{U}$[−1, 1]	$0.06^{+0.16}_{-0.17}$
Derived parameters for HD 3167c		
Planet mass $M_{\rm p}$ ($M_\oplus$)	...	$8.33^{+1.79}_{-1.85}$
Planet radius $R_{\rm p}$ ($R_\oplus$)	...	$2.740^{+0.106}_{-0.100}$
Mean density $\rho_{\rm c}$ (g cm^{-3})	...	$2.21^{+0.56}_{-0.53}$
Eccentricity e	...	$0.05^{+0.07}_{-0.04}$
Argument of periastron $w_\star$ (°)	...	178^{+134}_{-136}
Semimajor axis of the planetary orbit a (au)	...	0.1806 ± 0.0080
Orbit inclination $i_{\rm p}$ (°)	...	89.6 ± 0.2
Transit duration τ_{14} (hr)	...	$4.81^{+0.17}_{-0.09}$
Equilibrium temperature[b] $T_{\rm eq}$ (K)	...	548 ± 10
Signal with period of 10.7 days		
Period $P_{\rm orb}$ (days)	$\mathcal{U}$[9.4, 12.0]	$10.77^{+0.15}_{-0.13}$
Radial velocity semi-amplitude variation K(m s^{-1})	$\mathcal{U}$[0, 100]	$1.34^{+0.27}_{-0.28}$
Signal with period of 6.0 days		
Period $P_{\rm orb}$ (days)	$\mathcal{U}$[5.4, 6.5]	$5.967^{+0.038}_{-0.035}$
Radial velocity semi-amplitude variation K (m s^{-1})	$\mathcal{U}$[0, 100]	1.26 ± 0.25
Other parameters		
Systemic velocity $\gamma_{\rm HARPS}$ (km s^{-1})	$\mathcal{U}$[19.4183, 19.6317]	19:52311 ± 0:00029
Systemic velocity $\gamma_{\rm HARPS-N}$ (km s^{-1})	$\mathcal{U}$[19.4086, 19.6197]	19:51471 ± 0:00036
RV jitter term $\sigma_{\rm HARPS}$ (m s^{-1})	$\mathcal{U}$[0, 10]	$1.44^{+0.24}_{-0.21}$
RV jitter term $\sigma_{\rm HARPS-N}$ (m s^{-1})	$\mathcal{U}$[0, 10]	$0.95^{+0.24}_{-0.20}$
Parameterized limb-darkening coefficient[c] q_1	$\mathcal{U}$[0, 1]	$0.34^{+0.26}_{-0.15}$
Parameterized limb-darkening coefficient[c] q_2	$\mathcal{U}$[0, 1]	$0.47^{+0.29}_{-0.22}$
Linear limb-darkening coefficient u_1	...	$0.54^{+0.15}_{-0.17}$
Quadratic limb-darkening coefficient u_2	...	$0.04^{+0.35}_{-0.27}$

Notes.
[a] $\mathcal{U}[a, b]$ refers to uniform priors between a and b, $\mathcal{N}[a, b]$ to Gaussian priors with mean a and standard deviation b, and $\mathcal{F}[a]$ to a fixed a value.
[b] Assuming zero albedo.
[c] Following Kipping (2013)'s limb-darkening parametrization.

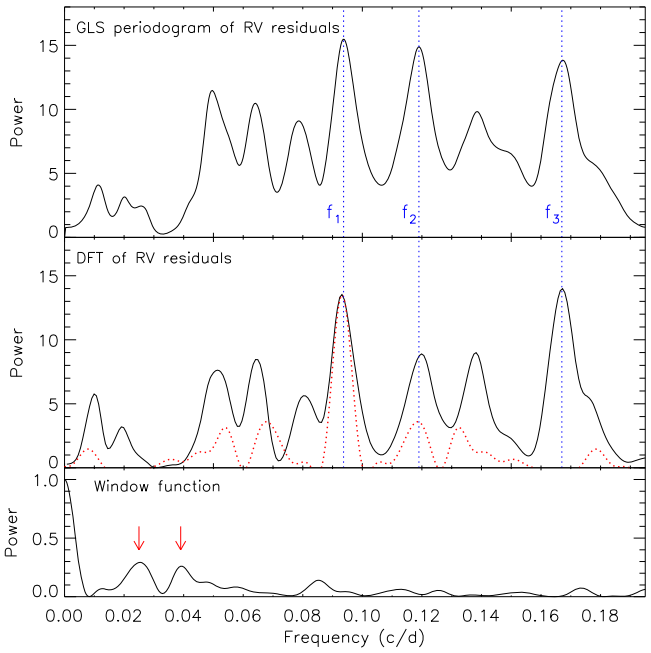

Figure 6. Top panel: GLS periodograms of the HARPS and HARPS-N RV residuals. The vertical dashed blue lines mark the frequencies $f_1 = 0.094$ c/d, $f_2 = 0.119$ c/d, and $f_3 = 0.167$ c/d whose FAP is less than 10^{-4}, as derived using a bootstrap randomization procedure. Middle-panel: Discrete Fourier transform of the HARPS and HARPS-N RV residuals. The dotted red line marks the window function shifted to the right by $f_1 = 0.094$ c/d and mirrored to the left of this frequency. Lower panel: Window function. The red arrows mark the two peaks presented in the main text.

orbital periods through *Kepler*'s third law. We did not add RV jitter terms at this stage of our analysis.

We explored the parameter space with 500 independent chains created from random priors for each parameter, as listed in the second column of Table 4. The convergence of the MCMC chains was checked with the Gelman–Rubin statistic. Once all chains converged, we ran 25,000 more iterations with a thin factor of 50. This led to a posterior distribution of 250,000 independent points for each fitted parameter.

The two-planet model provides a poor fit to the HARPS and HARPS-N measurements with an RV χ^2 of 597 and $\chi^2/\mathrm{dof} = 8.7$, suggesting that additional signals might be present in the data, as discussed in the next section.

5.4. Frequency Analysis of the RV Residuals

After fitting the two transiting planets, we inspected the RV residuals to look for additional signals in the Doppler data. The upper panel of Figure 6 shows the GLS periodogram of the RV residuals (thick black line). There are three significant peaks at $f_1 = 0.094$ c/d ($P_1 = 10.7$ days), $f_2 = 0.119$ c/d ($P_2 = 8.4$ days), and $f_3 = 0.167$ c/d ($P_3 = 6.0$ days). We assessed their FAP following the Monte Carlo bootstrap method described in Kürster et al. (1997). We computed the GLS periodograms of 10^4 fake data sets obtained by randomly shuffling the RV measurements, keeping the observation time-stamps fixed. The FAP is defined as the fraction of those periodograms whose highest power exceeds the power spectrum of the original observed data at any frequency. We found no false positives out of our 10^4 trials, implying that f_1, f_2, and f_3 have an FAP lower than 10^{-4}.

As a sanity check, we employed the program `Period04` (Lenz & Breger 2004) to calculate the discrete Fourier transform (DFT) of the RV residuals. We used the pre-whitening technique (see, e.g., Hatzes et al. 2010) to subsequently identify significant peaks in the power spectrum and remove the corresponding signal from the data. Briefly, we performed a least-squares sine-fit to the amplitude and phase at the first dominant frequency found by the DFT and subtracted the fit from the time series. We then reiterated the process to identify and subtract the next dominant Fourier component. The iteration was stopped once we reached the level of the noise. We regarded as significant only those signals whose amplitudes are more than four times the Fourier noise level (Breger et al. 1993). The Fourier fit of the RV residuals was obtained with only two dominant frequencies, namely, $f_1 = 0.094$ c/d and $f_3 = 0.167$ c/d, with an amplitude of 1.4 and 1.1 m s^{-1}, respectively.

The periodogram of the sampling pattern—the so-called "window function"—shows two peaks at 0.025 c/d (40 days) and 0.039 c/d (25 days). They are highlighted by two red arrows in the lower panel of Figure 6. We note that the beat frequency between $f_1 = 0.094$ c/d and $f_2 = 0.119$ c/d is equal to 0.025 c/d, which corresponds to one of the two frequencies seen in the window function. This led us to suspect that f_1 and f_2 are aliases of one another and share the same physical origin. We verified this hypothesis using again the pre-whitening technique. We performed a least-squares sine-fit to the amplitude and phase at either f_1 or f_2, subtracted the best fit from the RV time series, and recalculated the GLS periodogram of the new residuals. Regardless of which of the two signals is fitted and subtracted first, by removing one of the two, we also remove the other, as expected from alias peaks, confirming our hypothesis. We note that the subtraction of the signal at either f_1 or f_2 does not remove $f_3 = 0.167$ c/d, which remains significant in the GLS periodogram of the new residuals.

The middle panel of Figure 6 shows the DFT of the RV residuals (thick black line), along with the window function shifted to the right by $f_1 = 0.094$ c/d and mirrored to the left of this frequency (red dotted line). It is evident that f_2, along with most of the side lobes seen to the right and left of f_1, is an alias of the latter related to the observing window. We conclude that f_1 is very likely the actual periodicity. We also note that f_3 is not an alias of f_1, as there is no peak detected in the "shifted" window function at this frequency, corroborating our pre-whitening analysis.

To further assess which of the two signals is the actual periodicity, we performed a least-squares multi-sine fit to the amplitude and phase at the frequency couples f_1, f_3, and f_2, f_3. We then created synthetic RV residuals using the best-fitting parameters, added white noise, sampled the simulated data at the epochs of our real observations, and calculated the GLS periodograms. We found that "fake" data sets obtained from the couple f_1, f_3 reproduce the observed periodogram better than the couple f_2, f_3. This further supports the fact that the RV residuals contain only two significant signals at $f_1 = 0.094$ c/d ($P_1 = 10.7$ days) and $f_3 = 0.167$ c/d ($P_3 = 6.0$ days).

What are the sources of the two signals at 6.0 and 10.7 days detected in the RV residuals? Are they due to activity, additional planets, or both? Given the history of misinterpretation of stellar activity signals as planets near harmonics of the rotation period (see, e.g., Robertson et al. 2014, 2015), due

Table 5
FIES, HARPS, and HARPS-N Radial Velocity Measurements and Activity Indicators of HD 3167

BJD_{TDB} −2,450,000	RV (km s^{-1})	σ_{RV} (km s^{-1})	CCF BIS (km s^{-1})	CCF FWHM (km s^{-1})	$\log R'_{HK}$ (dex)	$\sigma_{\log R'_{HK}}$ (dex)	S/N per pixel @ 5500 Å
FIES							
7598.642079	0.0041	0.0024	⋯	⋯	⋯	⋯	89.2
7598.722300	−0.0016	0.0022	⋯	⋯	⋯	⋯	94.3
7599.670737	0.0074	0.0022	⋯	⋯	⋯	⋯	90.2
7599.734782	0.0040	0.0018	⋯	⋯	⋯	⋯	99.8
7601.612462	0.0104	0.0031	⋯	⋯	⋯	⋯	78.3
7601.725746	0.0071	0.0020	⋯	⋯	⋯	⋯	95.0
7605.728060	0.0000	0.0025	⋯	⋯	⋯	⋯	108.3
7619.630231	0.0074	0.0022	⋯	⋯	⋯	⋯	93.2
7619.732981	0.0047	0.0018	⋯	⋯	⋯	⋯	100.1
7622.572954	0.0093	0.0024	⋯	⋯	⋯	⋯	86.3

(This table is available in its entirety in machine-readable form.)

caution is warranted in the interpretation of these two signals. We note that the two periods $P_1 = 10.7$ days and $P_3 = 6.0$ days are close to the first and third harmonic of the rotational period of the star ($P_{rot} = 23.52 \pm 2.87$ days). This might lead us to suspect that magnetic activity coupled with stellar rotation is the source of the two additional signals. Active regions separated by ∼90 and ∼180 degrees in longitude could account for the two periodicities. To further investigate this hypothesis, we calculated the GLS periodograms of the activity indicators—namely, the FWHM and BIS of the cross-correlation profile, and the Ca II H & K activity index ($\log R'_{HK}$)—but found no significant peak. We stress, however, that this cannot be used to exclude that activity is the source of the observed RV variation. Given the amplitude of the two signals (1.2 and 1.4 m s^{-1}) and low projected rotational velocity of the star (1.8 ± 0.4 km s^{-1}), the suppression of granular blueshift in magnetized regions of the photosphere of HD 3167 is expected to be the source of the observed "jitter". Based on observations of the Sun as a star, Haywood et al. (2016) recently found that the traditional activity indicators perform poorly in tracing the RV jitter of slowly rotating stars with a low level of magnetic activity, such as in the case of HD 3167.

We further investigated the nature of the additional signals detected in the RV residuals using the stacked Bayesian generalized Lomb–Scargle (BGLS) periodogram proposed by Mortier & Collier Cameron (2017). This tool exploits the BGLS algorithm described in Mortier et al. (2015), which in turn is a Bayesian version of the GLS periodogram of Zechmeister & Kürster (2009). As described in Mortier & Collier Cameron (2017), the stacked BGLS periodogram relies on the assumption that the power (or probability) of a coherent RV signal—such as that produced by a bona fide orbiting planet—is expected to increase by adding more data points. On the contrary, the RV signal produced by stellar activity is usually incoherent, since its amplitude, phase, and period vary with time, due to the evolution of active regions, differential rotation, and magnetic cycle. Its significance can thus increases or decreases as more RV measurements are added to the data set. The tool calculates the BGLS periodogram for the first n out of N RVs (where $n \leqslant N$), adds the next point, recalculates the BGLS periodogram, and iterates the process until the last available measurement.

Figure 7 shows the BGLS periodogram (upper panel) and the stacked BGLS periodogram (lower panel) of the HARPS and HARPS-N RV residuals. As expected, the two dominant peaks at 6.0 and 10.7 days are clearly visible along with their aliases related to the observing window. We note that both signals do not seem to show a steadily increasing power (or probability) as we would expect from signals arising from the presence of planets. Is this enough to claim that the two periodic signals are due to activity? Following Johnson et al. (2016), we created a data set of synthetic RV residuals containing two sinusoidal signals at the same period, phase, and amplitude as the observed data. We added Gaussian noise and sampled the simulated RVs at the time stamps of our observations.

The BGLS periodogram and stacked BGLS periodogram of the synthetic data are shown in Figure 8. As is evident from a visual inspection, Figures 7 and 8 share roughly the same peaks and a similar pattern. None of the two simulated coherent signals shows a steadily increasing power. Given the data, this simulation proves that our sampling of two truly coherent signals at 6.0 and 10.7 days can mimic the trend expected from activity-induced RV variation in the stacked BGLS periodogram.

We conclude that, although we found evidence that there are two additional signals with periods of 6.0 and 10.7 days in the HARPS and HARPS-N measurements, the sampling of our observations, as well as the limited number of RVs and their noise level do not allow us to assess whether the two signals are due to activity, or are rather induced by two additional orbiting planets. We thus include the two signals in our analysis (Section 6) but warn the reader that more observations are needed to unveil their true nature.

6. Results

We used the code `pyaneti` to perform the final joint modeling of the *K2* and RV measurements. We fitted the transit and RV curves of HD 3167b and c following the guidelines presented in Section 5.3, and incorporated the modeling of the two additional RV signals at 6.0 and 10.7 days using two sinusoidal curves. We set uniform priors for the periods of the two additional signals—using a 2 day range centered around the values found by the frequency analysis presented in Section 5.4—and adopted uninformative priors over a wide range for the corresponding phases and amplitudes. To account for additional instrumental noise not included in the nominal RV error bars and/or imperfect treatment of the various sources of RV variations (e.g., stellar activity and/or additional

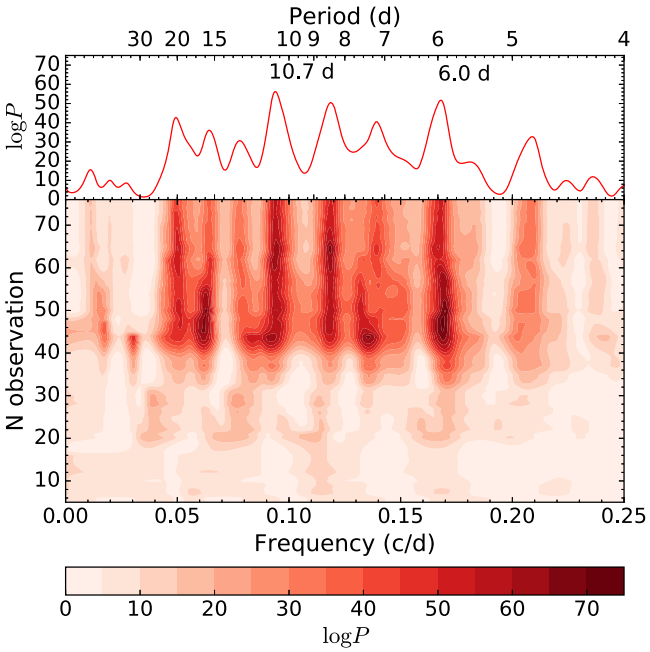

Figure 7. BGLS periodogram (upper panel) and stacked BGLS periodogram (lower panel) of the HARPS and HARPS-N RV residuals.

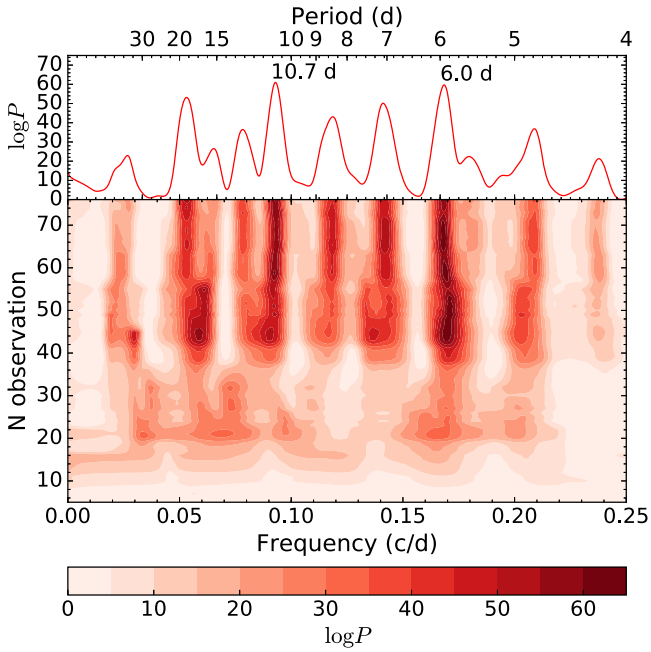

Figure 8. BGLS periodogram (upper panel) and stacked BGLS periodogram (lower panel) of the simulated HARPS and HARPS-N RV residuals.

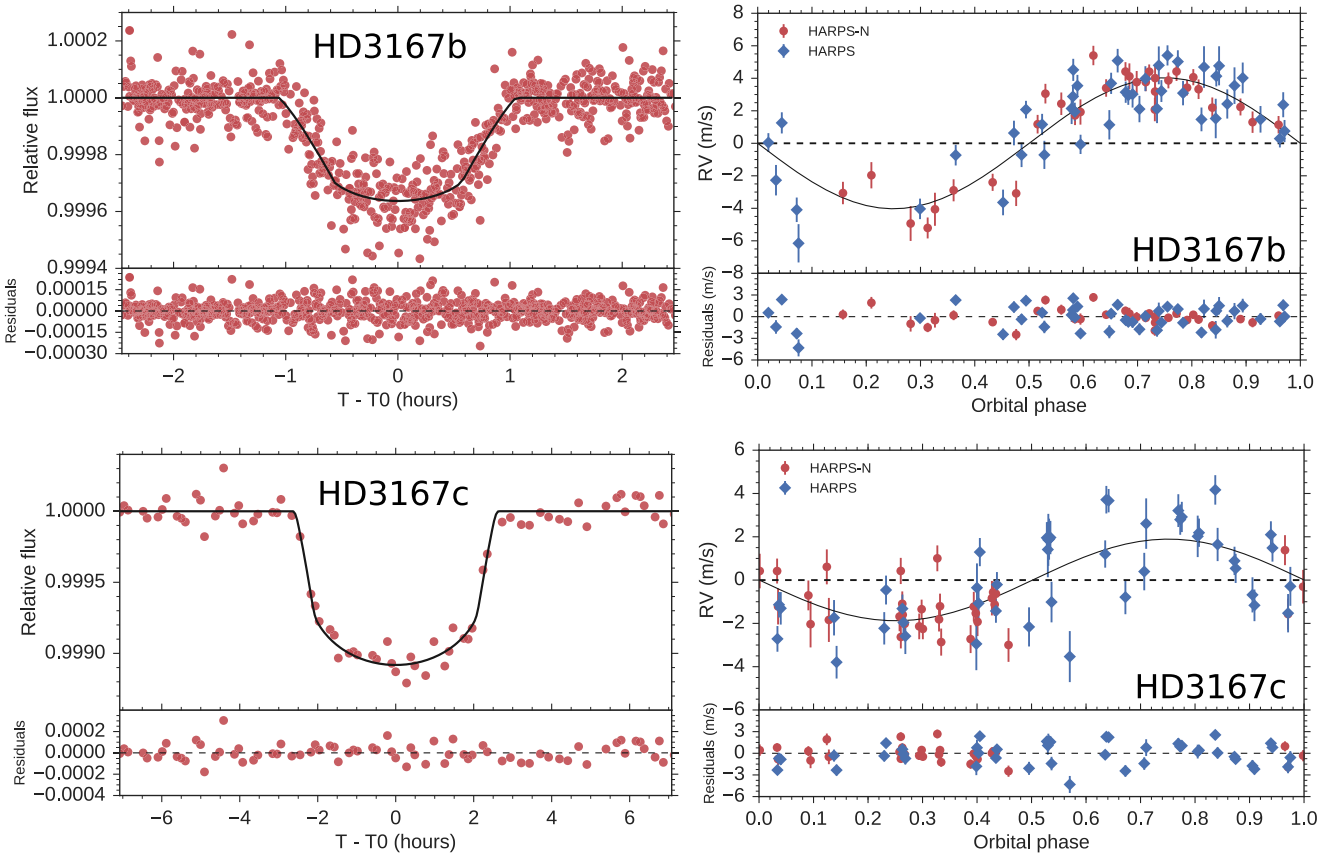

Figure 9. Transit light curves and RV curves of HD 3167 due to planet b (upper panels) and c (lower panels). The best-fitting transit and Keplerian models are overplotted with thick black lines. The *K2* data points are shown with red circles (left panels). The HARPS and HARPS-N RV measurements are plotted with red circles and blue diamonds, respectively, along with their nominal uncertainties (right panels). The RV curves are phase-folded to the orbital period of the two planets, following the subtraction of the systemic velocities and other signals, except planets b (upper right panel) and c (lower right panel).

planets), we added jitter terms to the equation of the likelihood for the HARPS and HARPS-N RV data following the method described in Dumusque et al. (2014).

We report our results in Table 4. The parameter estimates and their error bars were taken to be the median and the 68% credible interval of the final posterior probability distribution of each parameter. Figure 9 shows the *K2* transit light curves and best-fitting transit models, as well as the HARPS and HARPS-N RVs and best-fitting Keplerian models of HD 3167b and c. The RV fits to the two additional signals at 6.0 and 10.7 days are shown in Figure 10.

The mass of HD 3167b is in very good agreement with the value we derived using the FCO method corroborating our analysis (see Section 5.2). Similarly, the RV offset between HARPS and HARPS-N ($\Delta\,\mathrm{RV_{(HS\text{-}HN)}} = 8.3 \pm 0.2\,\mathrm{m\,s^{-1}}$) agrees with the value presented in Section 5.1 ($\Delta\,\mathrm{RV_{(HS\text{-}HN)}} = 8.0 \pm 0.5\,\mathrm{m\,s^{-1}}$). Finally, our values of the planetary radii agree within less than 1σ with those found by Vanderburg et al. (2016).

Does the inclusion of the 6.0 and 10.7 day signals bias the mass determinations of HD 3167b and HD 3167 c? A two-planet model fit that includes only planets b and c gives RV semi-amplitude variations of $K_\mathrm{b} = 3.74 \pm 0.39\,\mathrm{m\,s^{-1}}$ and $K_\mathrm{c} = 2.29 \pm 0.45\,\mathrm{m\,s^{-1}}$, respectively. By adding only the 10.7 day signal, we get $K_\mathrm{b} = 4.06 \pm 0.37\,\mathrm{m\,s^{-1}}$ and $K_\mathrm{c} = 2.04 \pm 0.43\,\mathrm{m\,s^{-1}}$. By adding both the 10.7 day and the 6.0 day signal, we obtain $K_\mathrm{b} = 4.02 \pm 0.31\,\mathrm{m\,s^{-1}}$ and $K_\mathrm{c} = 1.88^{+0.40}_{-0.42}\,\mathrm{m\,s^{-1}}$, proving that the RV semi-amplitude variations—and thus the determination of the planetary masses of HD 3167b and HD 3167c—are not significantly affected by the inclusion of the two additional signals.

7. Discussion and Summary

The ultra-short-period planet HD 3167b has a mass of $M_\mathrm{b} = 5.69 \pm 0.44\,M_\oplus$ and a radius of $R_\mathrm{b} = 1.574 \pm 0.054\,R_\oplus$, yielding a mean density of $\rho_\mathrm{b} = 8.00^{+1.10}_{-0.98}\,\mathrm{g\,cm^{-3}}$. Figure 11 displays the position of HD 3167b on the mass–radius diagram compared to the sub-sample of small transiting planets ($R \leqslant 4\,R_\oplus$) whose masses and radii have been derived with a precision better than 20%. Theoretical models from Zeng et al. (2016) are overplotted using different lines and colors. The precision of our mass determination (∼8%) allows us to conclude that HD 3167b is a rocky terrestrial planet with a composition consisting of ∼50% silicate and ∼50% iron.

HD 3167b adds to the sample of low-mass, close-in planets with an RV-determined mass and a bulk density suggestive of a mostly rocky composition. Planets belonging to this sample have a restricted Jeans escape parameter $\Lambda \lesssim 20$ (Table 3). This parameter, defined as

$$\Lambda = \frac{G M_\mathrm{pl} m_\mathrm{H}}{k_\mathrm{B} T_\mathrm{eq} R_\mathrm{pl}}, \qquad (1)$$

was introduced by Fossati et al. (2017) who found that the hydrogen-dominated atmospheres of exoplanets with $\Lambda \lesssim 20$ lie in the "boil-off" regime (Owen & Wu 2016; Cubillos et al. 2017), where the escape is driven by the atmospheric thermal energy and low planetary gravity. Fossati et al. (2017) also found that the atmosphere of hot ($T_\mathrm{eq} \gtrsim 1000$ K), low-mass ($M_\mathrm{p} \lesssim 5\,M_\oplus$) planets with $\Lambda \lesssim 20$ shrinks to smaller radii so that their atmosphere evolves out of the "boil-off" regime in less than about 500 Myr.

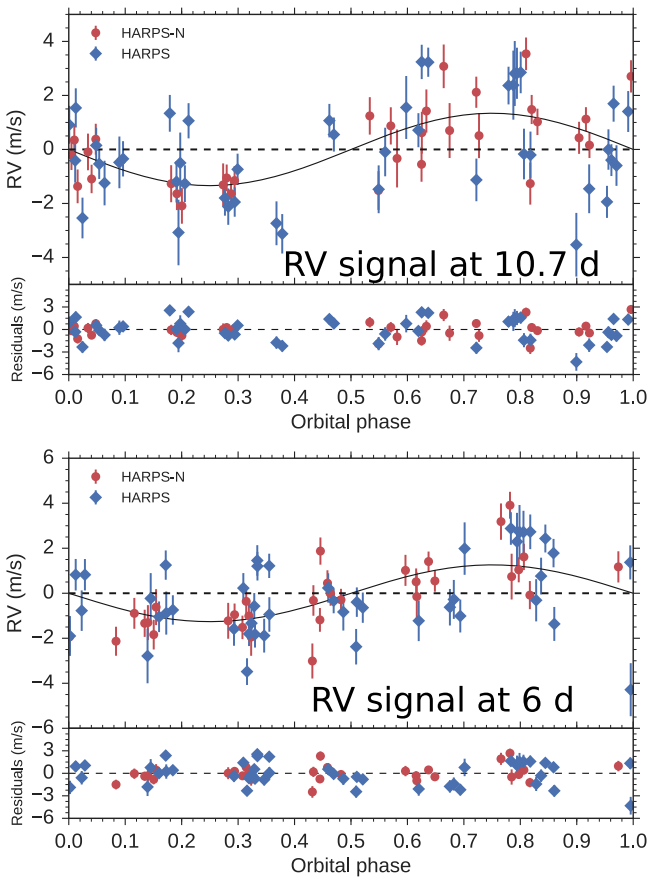

Figure 10. Radial velocity curves of the two signals at 10.7 days (upper panel) and 6.0 days (lower panel) and best-fitting models. The HARPS and HARPS-N RV measurements are plotted with red circles and blue diamonds, respectively, along with their nominal uncertainties.

Because of the very large escape rates after the dispersal of the proto-planetary disk, planets such as HD 3167b have quickly lost (within a few hundred megayears) their primary hydrogen-dominated atmosphere, as supported, e.g., by the non-detection of a hydrogen exosphere around the ultra-short-period planet 55 Cnc e (Ehrenreich et al. 2012). We remark that this fast escape is not driven by the high-energy stellar flux, but by the high temperature of the lower atmosphere and low planetary gravity. This implies that these planets subsequently developed a secondary, possibly CO_2-dominated, atmosphere while the host star was still young and hence active. This led to the fast escape—this time instead driven by the high-energy stellar flux—also of the secondary atmosphere (Kulikov et al. 2006; Tian 2009), leaving behind the strongly irradiated rocky surface. It is therefore foreseeable that the high surface temperature led then to the formation of magma oceans on the day side (Miguel et al. 2011; Demory et al. 2016), which out-gases and sputters minerals, forming a tenuous atmosphere that is not too dissimilar from that of Mercury (e.g., Pfleger et al. 2015). Over time, lighter elements escape from the atmosphere, leaving behind a possibly extended exosphere composed mostly by heavy refractory elements that could be detected in transit at ultraviolet and optical wavelengths. This picture would be reinforced if the orbit of HD 3167b had a non-zero eccentricity, as this would lead to tidal heating and thus to

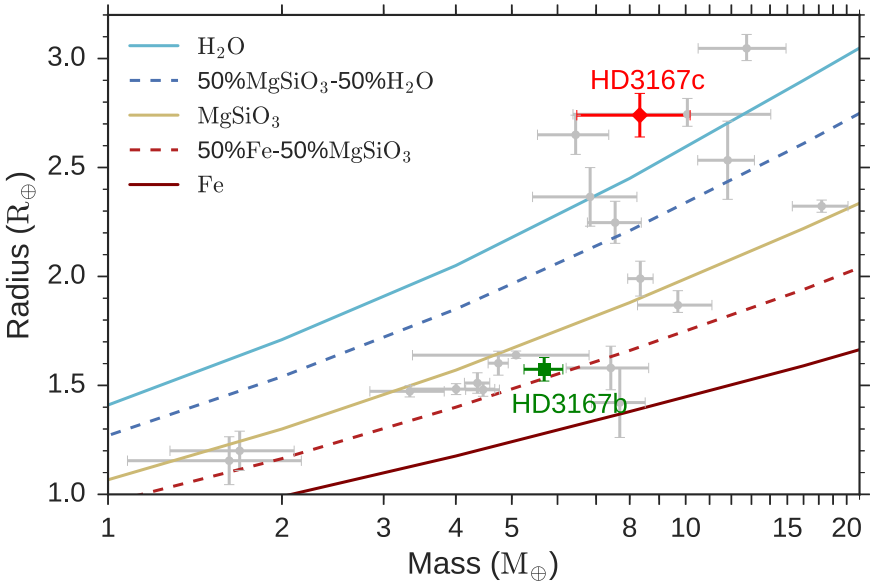

Figure 11. Mass–radius diagram for well-characterized (5σ precision level or better) super-Earths and -Neptunes. From bottom to top, the solid and dashed curves are theoretical models (Zeng et al. 2016) for planets with a composition of 100% iron (solid brown), 50% silicate and 50% iron (dashed red), 100% silicate (solid beige), 50% silicate and 50% water (dashed blue), and 100% water (solid light blue). HD 3167b and HD 3167c are highlighted with different symbols and colors.

a more extended magma ocean. The detection of the exosphere would then enable the study of the mineralogy of a rocky planet orbiting a star other than the Sun.

With a mass of $M_c = 8.33^{+1.79}_{-1.85}$ $M_\oplus$ and a radius of $R_c = 2.740^{+0.106}_{-0.100}$ $R_\oplus$ the outer planet HD 3167c has a mean density of $\rho_b = 2.21^{+0.56}_{-0.53}$ g cm^{-3}, which is consistent with a composition comprising a solid core surrounded by a thick atmosphere. HD 3167c joins the small group of low-density mini-Neptunes with precise mass and radius determinations (Figure 11).

HD 3167c is expected to have a completely different nature with respect to the inner planet b. Despite the lack of mass measurements, Vanderburg et al. (2016) noticed that HD 3167c may be a primary target for transmission spectroscopy. The rather large pressure scale height of about 350 km and the brightness of the host star ($V = 8.9$ mag) make HD 3167c an ideal target for transmission spectroscopy observations across a wide range of wavelengths, from the FUV to the infrared. One can expect the planet to have a rather large hydrogen-rich cloud made of gas escaping from the planetary upper atmosphere under the effect of the high-energy stellar radiation, similarly to GJ 436 b (Kulow et al. 2014; Ehrenreich et al. 2015). This cloud would be detectable at Lyα during primary transit. Such observations would then provide us with crucial information about the properties of the upper planetary atmosphere and its environment (e.g., stellar wind density and velocity). Observations at longer wavelengths would instead give us the opportunity to study the lower atmosphere and infer its chemical composition and physical properties. HD 3167c appears to be one of the best candidates to investigate the atmosphere of a low-mass planet.

We found evidence for two additional signals with periods of 10.7 and 6.0 days in the HARPS and HARPS-N data. The respective RV semi-amplitude variations are $1.34^{+0.27}_{-0.28}$ m s^{-1} and 1.26 ± 0.25 m s^{-1}. If the signals were caused by two additional orbiting planets, their minimum masses would be $4.24^{+0.87}_{-0.89}$ $M_\oplus$ and 3.28 ± 0.65 $M_\oplus$, respectively. According to the forecasting model of Chen & Kipping (2017), the two putative planets would have radii of $\sim$1.9 and 1.5 $R_\oplus$, implying that *K2* would have likely detected their transits if the two planets were transiting HD 3167. We searched the light curve for additional transit signals using the `DST` code of Cabrera et al. (2012), but found none. The null detection of the transits of the two putative additional planets requires that their orbits are inclined by at least 2°–3° relative to the orbits of planets b and c. Although a dynamical *N*-body simulation carried out with `mercury6` (Chambers 1999) shows that such a compact planetary system would be stable for at least 10^7 years, we stress again that our current data set does not allow us to assess whether the two signals are due to planets and/or activity. Additional RV observations are needed to unveil the real nature of the two signals.

This paper and the paper by Christiansen et al. (2017) were prepared simultaneously and are the result of independent RV observations and analyses of the HD 3167 system. We thank the anonymous referee for a thoughtful review and very positive feedback. We are extremely grateful to the NOT, ESO, and TNG staff members for their unique and superb support during the observations. We thank Xavier Bonfils, François Bouchy, Martin Kürster, Jorge Melendez, and Nuno Santos who kindly agreed to exchange HARPS time with us. D.G. would like to acknowledge the inspiring discussions with Conny Konnopke, Nuccio Lanza, Paul Robertson, Rodrigo Diaz, Elisa Delgado Mena, and Aldo Bonomo. D.G. gratefully acknowledges the financial support of the *Programma Giovani Ricercatori—Rita Levi Montalcini—Rientro dei Cervelli (2012)* awarded by the Italian Ministry of Education, Universities and Research (MIUR). M.F. and C.M.P. acknowledge generous support from the Swedish National Space Board. L.F. acknowledges the Austrian Forschungsförderungsgesellschaft FFG project "TAPAS4CHEOPS" P853993. S.z.C. thanks the Hungarian OTKA Grant K113117. H.J.D. and D.N. acknowledge support from grant ESP2015-65712-C5-4-R of the Spanish Secretary of State for R& D&i (MINECO). This research was supported by the Ministerio de Economia y Competitividad under project FIS2012-31079. JIGH and ASM acknowledge financial support from the Spanish Ministry project MINECO

AYA2014-56359-P, and J.I.G.H. also from the Spanish MINECO under the 2013 Ramón y Cajal program MINECO RYC-2013-14875. The research leading to these results has received funding from the European Union Seventh Framework Programme (FP7/2013-2016) under grant agreement No. 312430 (OPTICON). Based on observations obtained (a) with the Nordic Optical Telescope (NOT), operated on the island of La Palma jointly by Denmark, Finland, Iceland, Norway, and Sweden, in the Spanish Observatorio del Roque de los Muchachos (ORM) of the Instituto de Astrofísica de Canarias (IAC); (b) with the Italian Telescopio Nazionale Galileo (TNG) also operated at the ORM (IAC) on the island of La Palma by the INAF—Fundación Galileo Galilei; (c) the 3.6 m ESO telescope at La Silla Observatory under programs ID 097.C-0948 and 098.C-0860. This paper includes data collected by the *Kepler* mission. Funding for the *Kepler* mission is provided by the NASA Science Mission directorate.

Facilities: *Kepler* (K2), NOT (FIES), ESO-3.6 m (HARPS), TNG (HARPS-N).

Software: `IDL`, `SPECTRUM`, `SME`, `FAMA`, `DOOp`, `PARAM`, `pyaneti`, `exotrending`, `GLS`, `Period04`, `BGLS`, `DST`, `mercury6`.

ORCID iDs

Davide Gandolfi https://orcid.org/0000-0001-8627-9628
Oscar Barragán https://orcid.org/0000-0003-0563-0493
Malcolm Fridlund https://orcid.org/0000-0003-2180-9936
Luca Fossati https://orcid.org/0000-0003-4426-9530
Marshall C. Johnson https://orcid.org/0000-0002-5099-8185
Grzegorz Nowak https://orcid.org/0000-0002-7031-7754
Fei Dai https://orcid.org/0000-0002-8958-0683
Hans Deeg https://orcid.org/0000-0003-0047-4241
Michael Endl https://orcid.org/0000-0002-7714-6310
Joonas Saario https://orcid.org/0000-0003-0780-9825
Megan Bedell https://orcid.org/0000-0001-9907-7742
Pere Blay https://orcid.org/0000-0003-2018-1059
Juan Cabrera https://orcid.org/0000-0001-6653-5487
Felice Cusano https://orcid.org/0000-0003-2910-6565
William D. Cochran https://orcid.org/0000-0001-9662-3496
Jonay I. González Hernández https://orcid.org/0000-0002-0264-7356
Norio Narita https://orcid.org/0000-0001-8511-2981
Vincent Van Eylen https://orcid.org/0000-0001-5542-8870
Joshua N. Winn https://orcid.org/0000-0002-4265-047X

References

Aigrain, S., Parviainen, H., & Pope, B. J. S. 2016, MNRAS, 459, 2408
Baglin, A., & Fridlund, M. 2006, in The CoRoT Mission Pre-Launch Status—Stellar Seismology and Planet Finding, ESA-SP 1306, ed. M. Fridlund et al. (Noordwijk: ESA), 11
Barragán, O., & Gandolfi, D. 2017, Exotrending: Fast and easy-to-use light curve detrending software for exoplanets, Astrophysics Source Code Library, ascl:1706.001
Barragán, O., Gandolfi, D., Antoniciello, G., et al. 2017, pyaneti: Multi-planet radial velocity and transit fitting, Astrophysics Source Code Library, ascl:1707.003
Barragán, O., Gandolfi, D., Smith, A. M. S., et al. 2017, arXiv:1702.00691
Barragán, O., Grziwa, S., Gandolfi, D., et al. 2016, AJ, 152, 193
Borucki, W. J., Koch, D., Basri, G., et al. 2010, Sci, 327, 977
Breger, M., Stich, J., Garrido, R., et al. 1993, A&A, 271, 482
Bressan, A., Marigo, P., Girardi, L., et al. 2012, MNRAS, 427, 127
Bruntt, H., Bedding, T. R., Quirion, P.-O., et al. 2010, MNRAS, 405, 1907
Burke, C. J., Christiansen, J. L., Mullally, F., et al. 2015, ApJ, 809, 8
Cabrera, J., Csizmadia, S., Erikson, A., Rauer, H., & Kirste, S. 2012, A&A, 548, A44
Cantat-Gaudin, T., Donati, P., Pancino, E., et al. 2014, A&A, 562, A10
Castelli, F., & Kurucz, R. L. 2004, arXiv:astro-ph/0405087
Chabrier, G. 2001, ApJ, 554, 1274
Chambers, J. E. 1999, MNRAS, 304, 793
Chen, J., & Kipping, D. 2017, ApJ, 834, 17
Christiansen, J. L., Vanderburg, A., Burt, J., et al. 2017, AJ, 154, 122
Cosentino, R., Lovis, C., Pepe, F., et al. 2012, Proc. SPIE, 8446, 84461V
Csizmadia, S., Moutou, C., Deleuil, M., et al. 2011, A&A, 531, A41
Cubillos, P., Erkaev, N. V., Juvan, I., et al. 2017, MNRAS, 466, 1868
David, T. J., Hillenbrand, L. A., Petigura, E. A., et al. 2016, Natur, 534, 658
Demory, B.-O., Gillon, M., de Wit, J., et al. 2016, Natur, 532, 207
Doyle, A. P., Davies, G. R., Smalley, B., et al. 2014, MNRAS, 444, 3592
Dumusque, X., Bonomo, A. S., Haywood, R. D., et al. 2014, ApJ, 789, 154
Ehrenreich, D., Bourrier, V., Bonfils, X., et al. 2012, A&A, 547, A18
Ehrenreich, D., Bourrier, V., Wheatley, P. J., et al. 2015, Natur, 522, 459
Ford, E. B. 2006, ApJ, 642, 505
Fossati, L., Ayres, T. R., Haswell, C. A., et al. 2013, ApJL, 766, L20
Fossati, L., Erkaev, N. V., Lammer, H., et al. 2017, A&A, 598, A90
Fossati, L., France, K., Koskinen, T., et al. 2015, ApJ, 815, 118
Frandsen, S., & Lindberg, B. 1999, in Astrophysics with the NOT, Proc. Anot. Conf, ed. H. Karttunen & V. Piirola (Piikkio, Finland: Univ. Turku, Tuorla Observatory), 71
Fridlund, M., Gaidos, E., Barragán, O., et al. 2017, arXiv:1704.08284
Gandolfi, D., Alcalá, J. M., Leccia, S., et al. 2008, ApJ, 687, 1303
Gandolfi, D., Parviainen, H., Deeg, H. J., et al. 2015, A&A, 576, A11
Gandolfi, D., Parviainen, H., Fridlund, M., et al. 2013, A&A, 557, A74
Goodman, J., & Weare, J. 2010, Comm. App. Math. Comp. Sci., 5, 65
Gray, R. O., & Corbally, C. J. 1994, AJ, 107, 742
Grziwa, S., Gandolfi, D., Csizmadia, S., et al. 2016, AJ, 152, 132
Guenther, E. W., Barragan, O., Dai, F., et al. 2017, arXiv:1705.04163
Gustafsson, B., Edvardsson, B., Eriksson, K., et al. 2008, A&A, 486, 951
Hatzes, A., Fridlund, M., Nachmani, G., et al. 2011, ApJ, 743, 75
Hatzes, A. P. 2014, A&A, 568, A84
Hatzes, A. P., Dvorak, R., Wuchterl, G., et al. 2010, A&A, 520, A93
Hatzes, A. P. 2016, SSRv, 205, 267
Haywood, R. D., Collier Cameron, A., Unruh, Y. C., et al. 2016, MNRAS, 457, 3637
Heiter, U., Lind, K., Asplund, M., et al. 2015, PhyS, 90, 054010
Howard, A. W., Johnson, J. A., Marcy, G. W., et al. 2009, ApJ, 696, 75
Howell, S. B., Sobeck, C., Haas, M., et al. 2014, PASP, 126, 398H
Johnson, M. C., Endl, M., Cochran, W. D., et al. 2016, ApJ, 821, 74
Kipping, D. M. 2013, MNRAS, 435, 2152
Kulikov, Y. N., Lammer, H., Lichtenegger, H. I. M., et al. 2006, Planet. Space Sci., 54, 1425
Kulow, J. R., France, K., Linsky, J., & Loyd, R. O. P. 2014, ApJ, 786, 132
Kürster, M., Schmitt, J. H. M. M., Cutispoto, G., & Dennerl, K. 1997, A&A, 320, 831
Kurucz, R. L. 2013, ATLAS12: Opacity sampling model atmosphere program, Astrophysics Source Code Library, ascl:1303.024
Léger, A., Rouan, D., Schneider, J., et al. 2009, A&A, 506, 287
Lenz, P., & Breger, M. 2004, in IAU Symp. 224, The A-Star Puzzle, ed. J. Zverko et al. (Cambridge: Cambridge Univ. Press), 786
Lomb, N. R. 1976, Ap&SS, 39, 447
Lucy, L. B., & Sweeney, M. A. 1971, AJ, 76, 544
Luger, R., Agol, E., Kruse, E., et al. 2016, AJ, 152, 100
Magrini, L., Randich, S., Friel, E., et al. 2013, A&A, 558, A38
Mandel, K., & Agol, E. 2002, ApJ, 580L, 171M
Marcy, G. W., Weiss, L. M., Petigura, E. A., et al. 2014, PNAS, 111, 12655
Mayor, M., Pepe, F., Queloz, D., et al. 2003, Msngr, 114, 20
Mayor, M., & Queloz, D. 1995, Natur, 378, 355
McQuillan, A., Mazeh, T., & Aigrain, S. 2014, ApJS, 211, 24
Miguel, Y., Kaltenegger, L., Fegley, B., & Schaefer, L. 2011, ApJL, 742, L19
Mortier, A., & Collier Cameron, A. 2017, arXiv:1702.03885
Mortier, A., Faria, J. P., Correia, C. M., Santerne, A., & Santos, N. C. 2015, A&A, 573, A101
Nowak, G., Palle, E., Gandolfi, D., et al. 2017, AJ, 153, 131
Owen, J. E., & Wu, Y. 2016, ApJ, 817, 107
Pepe, F., Cameron, A. C., Latham, D. W., et al. 2013, Natur, 503, 377
Pfleger, M., Lichtenegger, H. I. M., Wurz, P., et al. 2015, PS&S, 115, 90
Queloz, D., Bouchy, F., Moutou, C., et al. 2009, A&A, 506, 303
Robertson, P., Mahadevan, S., Endl, M., & Roy, A. 2014, Sci, 345, 440
Robertson, P., Roy, A., & Mahadevan, S. 2015, ApJL, 805, L22
Ryabchikova, T. A., Pakhomov, Y. V., & Piskunov, N. E. 2011, KIzKU, 153, 61

Sanchis-Ojeda, R., Rappaport, S., Pallè, E., et al. 2015, ApJ, 812, 112
Sanchis-Ojeda, R., Rappaport, S., Winn, J. N., et al. 2014, ApJ, 787, 47
Scargle, J. D. 1982, ApJ, 263, 835
Shkolnik, E. L., Rolph, K. A., Peacock, S., & Barman, T. S. 2014, ApJL, 796, L20
Sneden, C., Bean, J., Ivans, I., Lucatello, S., & Sobeck, J. 2012, MOOG: LTE line analysis and spectrum synthesis, Astrophysics Source Code Library, ascl:1202.009
Stetson, P. B., & Pancino, E. 2008, PASP, 120, 1332
Suárez Mascareño, A., Rebolo, R., González Hernández, J. I., & Esposito, M. 2015, MNRAS, 452, 2745
Telting, J. H., Avila, G., Buchhave, L., et al. 2014, AN, 335, 41
Tian, F. 2009, ApJ, 703, 905
Valenti, J. A., & Fischer, D. A. 2005, ApJS, 159, 141
Valenti, J. A., & Piskunov, N. 1996, A&As, 118, 595
Van Eylen, V., Nowak, G., Albrecht, S., et al. 2016, ApJ, 820, 56
van Leeuwen, F. 2007, A&A, 474, 653
Vanderburg, A., Bieryla, A., Duev, D. A., et al. 2016, ApJL, 829, L9
Vanderburg, A., & Johnson, J. A. 2014, PASP, 126, 948
Winn, J. N., & Fabrycky, D. C. 2015, ARA&A, 53, 409
Zechmeister, M., & Kürster, M. 2009, A&A, 496, 577
Zeng, L., Sasselov, D. D., & Jacobsen, S. B. 2016, ApJ, 819, 127